

**The following resources related to this article are available online at [www.sciencemag.org](http://www.sciencemag.org) (this information is current as of November 12, 2009):**

**Updated information and services**, including high-resolution figures, can be found in the online version of this article at:

<http://www.sciencemag.org/cgi/content/full/326/5955/980>

**Supporting Online Material** can be found at:

<http://www.sciencemag.org/cgi/content/full/326/5955/980/DC1>

This article **cites 22 articles**, 1 of which can be accessed for free:

<http://www.sciencemag.org/cgi/content/full/326/5955/980#otherarticles>

This article has been **cited by** 1 articles hosted by HighWire Press; see:

<http://www.sciencemag.org/cgi/content/full/326/5955/980#otherarticles>

This article appears in the following **subject collections**:

Materials Science

[http://www.sciencemag.org/cgi/collection/mat\\_sci](http://www.sciencemag.org/cgi/collection/mat_sci)

Information about obtaining **reprints** of this article or about obtaining **permission to reproduce this article** in whole or in part can be found at:

<http://www.sciencemag.org/about/permissions.dtl>

is the highest; this corresponds to an essentially single-domain, tetragonal-like state of the sample, as exemplified by the uniform image contrast in the AFM images (Fig. 4, D and E). In contrast, at the lowest value of relative displacement, the AFM images (Fig. 4, B and C) show clear signatures of stripe-like image contrast, indicative of a mixed state. As shown in fig. S7, we have been able to reversibly switch it through the states shown in Fig. 4, B to D. We note that the absolute value of the local surface displacement is  $\sim 1$  to 2 nm per 85 nm of film thickness. This corresponds to an effective strain of 1.2 to 2.4%, which is of the same order of magnitude as the highest strains reported for the relaxor ferroelectrics. These relatively large and nonvolatile changes in surface displacements make this an attractive system for use in nanoscale data storage elements (such as probe-based data storage) and microscale actuators (28).

Our experimental and theoretical studies have revealed the ability of the BFO system to morph into allotropic modifications. These forms are stabilized through the epitaxial strain imposed by the substrate. Of particular interest from the piezoelectrics point of view is the mixed phase state of the films. The ability to reversibly convert the T phase to a mixture of T and R phases through the application of an electric field suggests a close resemblance to other well-known piezoelectrics such as the morphotropic phase boundary compositions in the PZT family and the PMN-PT family. Our observations support the notion that such strain-driven phase evolution is a generic feature, akin to chemically driven phase changes

that are now well established in the manganites, cuprates, and relaxors. Furthermore, the observation of the strain-driven phase changes in BFO should motivate a search for similar control in other related perovskite systems. Furthermore, this reversible interconversion is accompanied by substantial changes in the height of the sample surface (a few nanometers), thus making this potentially attractive for AFM probe-based data storage applications.

#### References and Notes

1. P. Groth, *Ann. Phys. Chem.* **217**, 31 (1870).
2. V. M. Goldschmidt, *Trans. Faraday Soc.* **25**, 253 (1929).
3. R. E. Newnham, *Mater. Res. Soc. Bull.* **22**, 20 (1997).
4. E. Dagotto, *Nanoscale Phase Separation and Colossal Magnetoresistance*, (Springer Verlag, New York, 2003).
5. S. E. Park, T. R. ShROUT, *J. Appl. Phys.* **82**, 1804 (1997).
6. R. Guo *et al.*, *Phys. Rev. Lett.* **84**, 5423 (2000).
7. H. Fu, R. E. Cohen, *Nature* **403**, 281 (2000).
8. M. Ahart *et al.*, *Nature* **451**, 545 (2008).
9. W. Eerenstein, N. D. Mathur, J. F. Scott, *Nature* **442**, 759 (2006).
10. R. Ramesh, N. A. Spaldin, *Nat. Mater.* **6**, 21 (2007).
11. C. Ederer, N. A. Spaldin, *Phys. Rev. Lett.* **95**, 257601 (2005).
12. P. Ravindran, R. Vidyaa, A. Kjekshus, H. Fjellvåg, *Phys. Rev. B* **74**, 224412 (2006).
13. D. Ricinchi, K.-Y. Yun, M. Okuyama, *J. Phys. Condens. Matter* **18**, L97 (2006).
14. H. Béa *et al.*, *Phys. Rev. Lett.* **102**, 217603 (2009).
15. D. G. Schlom *et al.*, *Annu. Rev. Mater. Res.* **37**, 589 (2007).
16. F. Zavaliche *et al.*, *Phase Transit.* **79**, 991 (2006).
17. G. Xu *et al.*, *Appl. Phys. Lett.* **86**, 182905 (2005).
18. Y. H. Chu *et al.*, *Appl. Phys. Lett.* **90**, 252906 (2007).
19. H. Béa *et al.*, *Phys. Rev. B* **74**, 020101 (2006).
20. K. Y. Yun *et al.*, *J. Appl. Phys.* **96**, 3399 (2004).
21. Materials and methods are available as supporting material on Science Online.

22. M. F. Chisholm *et al.*, *Microsc. Microanal.* **10**, 256 (2004).
23. G. Kresse, J. Furthmüller, *Phys. Rev. B* **54**, 11169 (1996).
24. V. I. Anisimov, F. Aryasetiawan, A. I. Liechtenstein, *J. Phys. Condens. Matter* **9**, 767 (1997).
25. A. G. Christy, *Acta Crystallogr. B* **51**, 753 (1995).
26. R. V. Shpanchenko *et al.*, *Chem. Mater.* **16**, 3267 (2004).
27. A. A. Belik *et al.*, *Chem. Mater.* **18**, 798 (2006).
28. S. Hong, Ed., *Nanoscale Phenomena in Ferroelectric Thin Films* (Kluwer Academic Publishing, Boston, MA, 2004).
29. The work at Berkeley is supported by the Director, Office of Science, Office of Basic Energy Sciences, Materials Sciences Division of the U.S. Department of Energy under contract DE-AC02-05CH11231. The authors from Berkeley acknowledge the support of the National Center for Electron Microscopy, Lawrence Berkeley National Laboratory. Y.H.C. also acknowledges the support of the National Science Council, R.O.C., under contract NSC 98-2119-M-009-016. V.G. and D.G.S. acknowledge support from National Science Foundation grants DMR-0820404 and DMR-0507146. A.H. and N.S. acknowledge support from the National Science Foundation under DMR-0820404 and NIRT-0609377. Theoretical work used the SGI Altix [Cobalt] system and the TeraGrid Linux Cluster [Mercury] at the National Center for Supercomputing Applications under grant DMR-0940420. C.E. acknowledges support from the Science Foundation of Ireland (grant SFI-07/Y12/I1051). The work of G.S. and L.Q.C. is supported by Department of Energy Basic Sciences under contract DE-FG02-07ER46417.

#### Supporting Online Material

www.sciencemag.org/cgi/content/full/326/5955/977/DC1  
Materials and Methods  
Figs. S1 to S8  
References

29 May 2009; accepted 1 September 2009  
10.1126/science.1177046

## Observation of the Role of Subcritical Nuclei in Crystallization of a Glassy Solid

Bong-Sub Lee,<sup>1,2</sup> Geoffrey W. Burr,<sup>3</sup> Robert M. Shelby,<sup>3</sup> Simone Raoux,<sup>3\*</sup> Charles T. Rettner,<sup>3</sup> Stephanie N. Bogle,<sup>1,2</sup> Kristof Darmawikarta,<sup>1,2</sup> Stephen G. Bishop,<sup>2,4</sup> John R. Abelson<sup>1,2,†</sup>

Phase transformation generally begins with nucleation, in which a small aggregate of atoms organizes into a different structural symmetry. The thermodynamic driving forces and kinetic rates have been predicted by classical nucleation theory, but observation of nanometer-scale nuclei has not been possible, except on exposed surfaces. We used a statistical technique called fluctuation transmission electron microscopy to detect nuclei embedded in a glassy solid, and we used a laser pump-probe technique to determine the role of these nuclei in crystallization. This study provides a convincing proof of the time- and temperature-dependent development of nuclei, information that will play a critical role in the development of advanced materials for phase-change memories.

The phase transformation of a material often starts with the formation of nanometer-sized volumes of the new phase, nuclei, which then grow in size. The nucleation process has been described by classical theory (1–3), in which the thermodynamic free energy is reduced by the phase transformation, whereas the formation of a nucleus involves an energy penalty associated with the boundary region between the

phases, particularly when atomic bonds are broken or strained. This interplay between volume and surface effects results in a critical nucleus size. For a subcritical nucleus, the energy rises as atoms are added to the new configuration; for a supercritical nucleus, the energy falls, because the energy reduction by phase transformation is now greater than the surface penalty. As thermal fluctuations induce atoms to join or leave each

subcritical nucleus, a size distribution of subcritical nuclei develops in the material. Only a minute fraction of subcritical nuclei achieve the critical size ( $n_c$ ) and continue to grow into a crystalline grain that is large enough to be detected by conventional analyses.

However, very few experimental studies have provided quantitative information on the distribution of nanoscale subcritical nuclei that develops before the observable phase transformation. Data are available only in very special cases, such as heteroepitaxial film growth where the nuclei are exposed on a flat surface (4, 5). On the micron length scale, nuclei and their behaviors can be observed in the agglomeration of colloidal particles in liquids (6, 7). The general case, such as crystallization from nanometer-scale nuclei that are embedded in the parent glassy phase,

<sup>1</sup>Department of Materials Science and Engineering, University of Illinois at Urbana-Champaign (UIUC), Urbana, IL 61801, USA. <sup>2</sup>Coordinated Science Laboratory, University of Illinois at Urbana-Champaign, Urbana, IL 61801, USA. <sup>3</sup>IBM/Macronix Phase Change Random Access Memory Joint Project, IBM Almaden Research Center, San Jose, CA 95120, USA. <sup>4</sup>Department of Electrical and Computer Engineering, University of Illinois at Urbana-Champaign, Urbana, IL 61801, USA.

\*Present address: IBM T. J. Watson Research Center, Yorktown Heights, NY 10598, USA.

†To whom correspondence should be addressed. E-mail: abelson@illinois.edu

offers substantial experimental challenges. X-ray diffraction fails to show the presence of these nuclei in the amorphous material, and the interpretation of image contrast in high-resolution transmission electron microscopy (TEM) has been shown to be unreliable for embedded objects smaller than  $\sim 3$  nm (8, 9).

This study combines a kinetic measurement, structural probe, and numerical simulation to reveal the presence of nanoscale subcritical nuclei in a glassy solid and their role in crystallization. For the detection of nuclei, we discover that a statistical technique, fluctuation TEM (FTEM), is a powerful tool. FTEM was originally devised to analyze topological order on the length scale of 1 to 4 nm, with spatial correlations beyond the nearest neighbor often called medium range order (10). In FTEM, hundreds of nanodiffraction patterns are obtained in a scanning transmission electron microscope and analyzed in terms of the scattering variance  $V(k)$ , where  $k$  is the scattering vector (11). It has been proven that this variance is mathematically related to a sum over three- and four-atom correlations in the material (9, 12), enabling the study of medium range order. Simulations with computational model structures (9, 12–14) have shown that one way to generate a realistic variance signal is by mixing ordered regions (e.g., crystalline nuclei) of a specified size and volume fraction in the parent random-network matrix. No alternative models have been identified yet, and the present study experimentally confirms the validity of the interpretation based on subcritical nuclei.

We find that Ag/In-incorporated  $\text{Sb}_2\text{Te}$  [known as AIST, technologically important for phase-change data storage (15, 16)] provides a nearly ideal system for the purpose of this study. We can systematically modify the population of subcritical nuclei embedded in amorphous AIST with the use of low-temperature thermal annealing or short laser pulses. The effect of such a pretreatment is not detectable in conventional diffraction measurements but is evidenced as follows: (i) We use a laser pump-probe technique to measure the time required for nucleation (the formation of a supercritical nucleus) and find significant enhancement or suppression of this nucleation time by pretreatment. (ii) We use FTEM to measure changes in the nanoscale structural order within the sample, and we show that these changes are consistent with the laser data. Finally, (iii) we simulate the kinetic process by which the size distribution of subcritical nuclei evolves, and we show that it is in good agreement with (i) and (ii).

To induce and monitor the crystallization process, we used a laser pump-probe technique (11, 17, 18). A focused pump laser heats a thin-film sample of amorphous AIST with specified power and duration, whereas a low-power probe laser monitors the optical reflectivity in real time during the process (Fig. 1A). Thermal simulations show that any particular portion of the irradiated area reaches a constant temperature in only  $\sim 10$  ns and also that the area cools in  $\sim 10$  ns

after the laser is turned off (fig. S1A). Because the beam intensity has a Gaussian spatial profile, the temperature is substantially higher at the center than at the edges of the spot. When held at an intermediate temperature for a suf-

ficient length of time, in this case under a pump laser of 40 to 60 mW ( $1/e^2$  diameter = 2  $\mu\text{m}$ ) for more than 80  $\mu\text{s}$ , the amorphous state crystallizes. This crystallization process can be detected in real time with the use of the probe laser, because

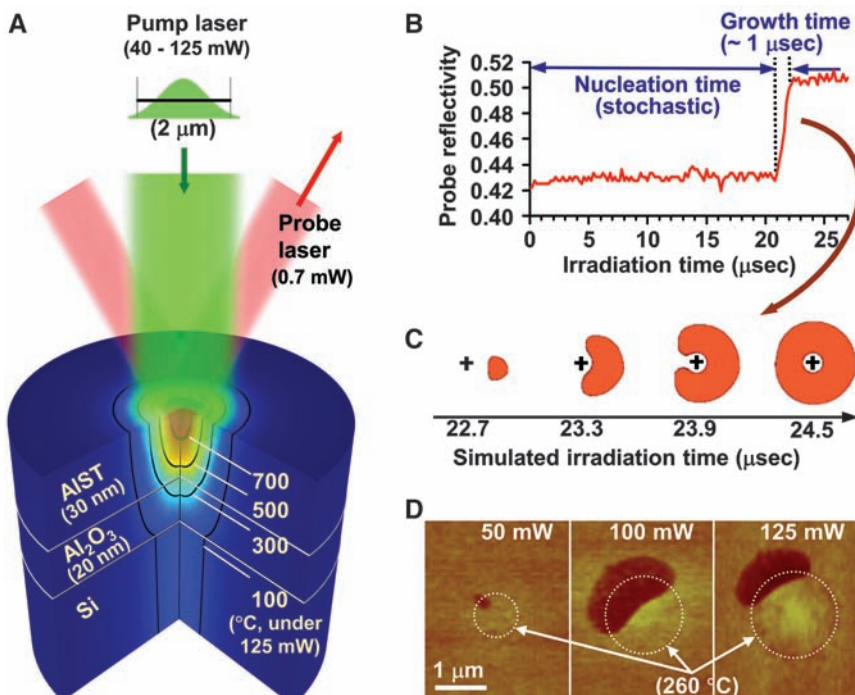


**Fig. 1.** Pump-probe laser analysis of nucleation in amorphous AIST (Ag/In-incorporated  $\text{Sb}_2\text{Te}$ ). (A) Experimental setup with a pump laser for heating and a probe laser (normal incidence in the real setup) for monitoring reflectivity in situ. The simulated steady-state temperature distribution under a Gaussian pump laser of 125 mW is inscribed. (B) Typical change in reflectivity that accompanies the laser crystallization of AIST, showing the time before a single supercritical nucleus appears, followed by rapid growth across the irradiated area, which increases the reflectivity. (C) Plan-view snapshots of simulated laser crystallization, in which the center temperature is near the melting point. (D) AFM images obtained after interrupted crystallization (dark contrast), where the pump laser was turned off after nucleation but before full crystallization. Laser crystallization of AIST proceeds from a single nucleus, which develops near an optimal temperature  $T_0 \sim 260^\circ\text{C}$  (dotted circles).

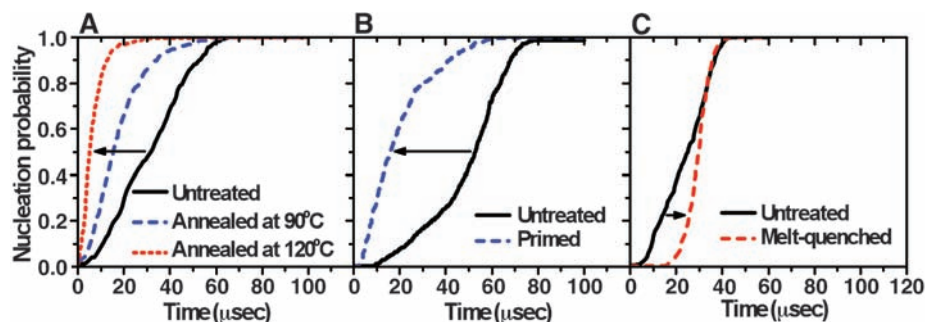


**Fig. 2.** Cumulative probability that nucleation occurs within a given time in AIST under pump laser. (A) Effect of low-temperature annealing. The nucleation time from a pre-annealed amorphous state is shorter than that from an untreated state (pump-laser power = 50 mW in these cases; the result was nearly insensitive to the choice of laser power between 40 and 60 mW). (B) Effect of laser priming. A short prepulse (1  $\mu\text{s}$ , 60 mW) does not induce crystallization, but, from such a primed area, nucleation generally occurs in a shorter time under the next pulse with the same power. (C) Effect of melt quenching. From a melt-quenched amorphous area produced by an intense prepulse (122 mW), nucleation occurs in a slightly longer time under the next pulse (40 mW) (11). The change in nucleation time originates from the modification of subcritical nuclei population by pretreatment, as proven by FTEM (Fig. 4) and supported by simulation (Fig. 3).

the crystalline phase has a higher optical reflectivity (by ~20% in the layered structure used here). Under a high laser power (~120 mW), the center of the spot exceeds the AIST melting temperature of 544°C (19). When the laser is turned off, the cooling time is sufficiently short to transform the liquid into the melt-quenched amorphous state.

The laser-induced crystallization of an irradiated area typically results from the formation—after an incubation delay (nucleation time)—of a single supercritical nucleus, which then rapidly grows across the entire hot zone (17). The nucleation time is measured via the reflectivity (Fig. 1B). The solid amorphous state attempts to create the first supercritical nucleus for many microseconds (constant reflectivity) and, after one supercritical nucleus forms, the crystallization front spreads across the irradiated area in only ~1  $\mu$ s (rapid increase in reflectivity). The nucleation time may range from 5 to 60  $\mu$ s in laser spots obtained on a single sample, which demonstrates the stochastic nature of nucleation. Figure 1C shows simulated plan-view snapshots (11) that illustrate the growth of a supercritical nucleus from an irradiated area; the center temperature is near the melting point in this case. Images similar to those in Fig. 1C can be experimentally obtained. Crystallization results in a ~5% volume contraction, and a crystallized area (if larger than tens of nanometers in lateral extent) can be detected via the associated thickness change in an atomic force microscopy (AFM) image [(20, 21), also see fig. S2A]. If the pump beam happens to terminate after nucleation but before full crystallization, then the transformation process comes to a halt and leaves a partly crystallized region (interrupted crystallization). Figure 1D presents examples of such regions (dark contrast), which are approximately centered on the location of the single nucleus.

The location at which nucleation occurs within an irradiated spot demonstrates the existence of an optimal nucleation temperature  $T_0$ , as predicted by classical theory. At low temperatures, the thermodynamic driving force for crystallization (the free energy difference between the two phases) is large, but the kinetic rate of atomic rearrangements is small. At high temperatures, the rate of rearrangements is large, but the driving force is small (that is, the critical nucleus size is large and difficult to attain). The nucleation rate reaches a sharp maximum at an intermediate temperature  $T_0$  (2, 22). Our numerical simulation of the nucleation process in AIST (11) suggests a maximum rate at ~260°C. In every case where interrupted crystallization was observed, the originating nucleus was located not far from the annulus where the temperature was 260°C [shown as dotted circles on Fig. 1D according to our temperature calculations (11), also see fig. S1B].

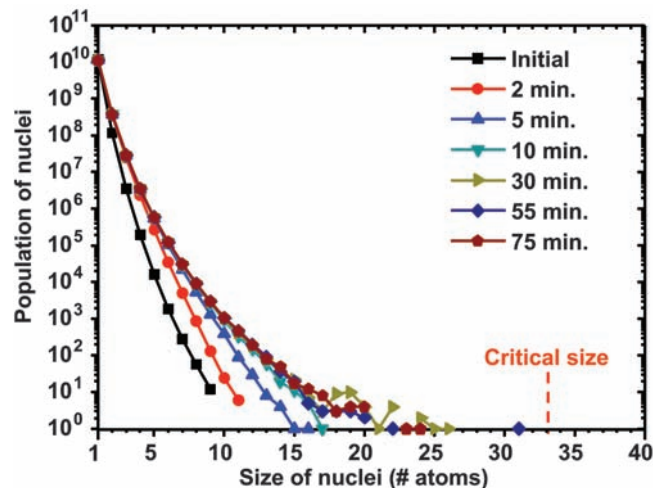
Statistical analysis reveals that the nucleation time of AIST can be systematically modified by a thermal pretreatment. Figure 2 presents the cu-

mulative probability that nucleation occurs within a given time. Each curve was obtained from 500 identical laser shots for ~100  $\mu$ s applied to a set of neighboring areas on one sample (11) and represents the distribution of stochastic nucleation times measured, as in Fig. 1B. Thermal annealing in a furnace for 30 min at 90° or at 120°C does not induce crystallization, but the laser-crystallization time in such a pre-annealed sample is statistically shorter (Fig. 2A) (17). The time for 50% nucleation probability was reduced from 32 (untreated) to 5  $\mu$ s (annealed at 120°C). Alternatively, the sample can be treated by a laser prepulse of the same power (e.g., 60 mW) that would eventually initiate crystallization, but of a duration (1  $\mu$ s) shorter than the time required for the onset of crystallization. This pretreatment, referred to as laser priming (23), also reduces the crystallization time [from 53 to 16  $\mu$ s (Fig. 2B)]. Thus, either long furnace annealing at low temperatures or short laser annealing at intermediate temperatures shortens the nucleation time. [In extreme cases where nucleation time was very much shortened, multiple supercritical nuclei could occur before full crystallization (fig. S2B).] On the other hand, a high-power (122-mW) prepulse can induce melt quenching. Figure 2C shows that the nucleation time from a melt-quenched amorphous region (30  $\mu$ s for 50%) is somewhat longer than that from untreated regions on the same sample (25  $\mu$ s). The nucleation time from the initial untreated states varies in different samples as shown by the continuous curves in Fig. 2, A to C (between 25 and 53  $\mu$ s for 50%), due to variations in the sample preparation conditions. Regardless, the effects of pre-annealing, laser priming, and melt quenching have been confirmed in a consistent manner from at least four samples in each case.

The observation that nucleation times can be shortened or lengthened by a thermal pretreatment indicates the presence of metastable configurations in the amorphous material. Nucleation

theory predicts that a size distribution of subcritical nuclei will develop and evolve according to the thermal history of the sample. To evaluate this, we employed a customized finite-difference simulation program (24), which models the stochastic evolution of subcritical nuclei via rate equations (18, 22), as well as the propagation of crystalline growth fronts as a function of time and temperature distribution over a three-dimensional Cartesian mesh with more than 370,000 simulation grid-cells (11). This simulation models a collection of identical atoms, each representative of the weighted average constituent atom in  $\text{Ag}_{5.5}\text{In}_{6.5}\text{Sb}_{65}\text{Te}_{29}$  (19); this is a reasonable approximation considering that the reported crystal structure of AIST is nearly identical to that of elemental antimony and also that the constituent atoms randomly occupy the atomic sites (25). A typical simulation (Fig. 1C) shows a satisfactory match to the experimental results. A supercritical nucleus forms after ~22  $\mu$ s, then grows in ~2  $\mu$ s. The distributions at 125°C (Fig. 3) report the total number of nuclei within the simulation volume of 3.5  $\mu$ m by 3.5  $\mu$ m by 30 nm. From a quasi-equilibrium state at 25°C, the distribution slowly shifts to a larger size, with the upper end (the maximum nucleus size) fluctuating by random attachment or detachment of atoms; the apparent small peaks at the upper end of the distribution are noise from this stochastic process. Supercritical nuclei may appear after tens of hours; they will then grow in size but at an extremely low rate. At high temperature under laser heating, the development of nuclei can occur in as little as 1  $\mu$ s (priming), followed by nucleation and growth (crystallization of the spot). In phase-change memory devices, the difference between a stored “1” and “0” data bit is the presence (or absence) of a small amorphous region. Therefore, the development of nuclei as in Fig. 3 and subsequent crystallization of the amorphous region is a possible mechanism to lose the stored data (26); the kinetics is highly

**Fig. 3.** Simulated evolution of nuclei size distribution in amorphous AIST at 125°C, which illustrates the effect of thermal pretreatment. The distribution of nuclei across a 3.5  $\mu$ m by 3.5  $\mu$ m by 30 nm volume of AIST is shown at various times after the simulated volume is instantaneously brought to 125°C. The initial nuclei distribution corresponds to the steady-state condition at 25°C. The total population of atoms not associated with clusters ( $n = 1$ ) decreases slightly over time, from  $1.20 \times 10^{10}$  to  $1.14 \times 10^{10}$  after 5 min. At higher temperatures (e.g., by laser priming), such evolution occurs on a shorter time scale. From a pretreated sample, the time to generate a supercritical nucleus under laser irradiation is shorter.



dependent on the temperature at the working environment.

The experimentally measured distributions of nucleation time (Figs. 1B and 2, A to C) reveal the time necessary for the upper end of the initial distribution of subcritical nuclei to fluctuate until at least one nucleus exceeds  $n_c$  at the temperature established by the pump laser. The average nucleation time is shorter after pre-annealing or priming (Fig. 2, A and B), because the upper end of the size distribution has already been moved up from the room-temperature distribution. When the sample is melted, all nuclei are dissolved. During a short cooling time ( $\sim 10$  ns), a distribution of subcritical nuclei again forms but only reaches small sizes before it is kinetically frozen at room temperature. Thus, the nucleation time from the melt-quenched state of AIST may be similar to or even longer than that from the untreated state (Fig. 2C). It is reasonable that a distribution of subcritical nuclei forms in the untreated state as a result of fast particle bombardment or energy dissipation during the sputter-deposition process (27). [If the development of nuclei is substantial during cooling from melt, the melt-quenched state may exhibit a shorter nucleation time. Such a reduced nucleation time is observed for the composition  $\text{Ge}_2\text{Sb}_2\text{Te}_5$  (17, 28). In the extreme case of a bad glass-former, the material will fully crystallize during cooling.]

Although the average electron diffraction intensity is unaltered by the pretreatments (fig. S3), FTEM clearly demonstrates the structural differences between pretreated states. A membrane structure was designed to allow both laser pretreatment and FTEM analysis (11); an area showing interrupted crystallization (Fig. 4A)

allows a precise comparison between different amorphous states. The center is in the melt-quenched amorphous state, the uncrystallized portion of the perimeter is in the primed (irradiated but not crystallized) state, and the regions well outside the laser irradiation remain in the untreated amorphous state. The FTEM data (Fig. 4B, obtained by statistical analysis of nanodiffraction patterns as in fig. S4) reveal substantially higher peak intensity (i.e., higher structural order) for the primed state. Similar trends of smaller magnitude are found when samples are subjected to furnace annealing (Fig. 4C). On the other hand, the signal (most importantly, the first peak at  $k \sim 0.32 \text{ \AA}^{-1}$ ) is similar or slightly lower in the melt-quenched state. It is clear that the increase and decrease of FTEM peaks are consistent with the expected change of nuclei distribution. Annealing or priming shifts the distribution to larger sizes, whereas melt quenching leaves the material in a glassy state with a smaller or similar size distribution. [We previously observed similar annealing effects with  $\text{Ge}_2\text{Sb}_2\text{Te}_5$  and AIST (17, 29) but did not systematically relate them to nucleation theory.]

Although quantitative interpretation of FTEM data is complex, general principles are given by our simulation of the FTEM peak structure from a family of amorphous silicon models (13). The number of ordered regions mainly controls the magnitude of the FTEM peaks, whereas the mean size is related to the ratio in heights of the second and first peaks. The data in Fig. 4C then indicate mostly an increase in the number of such clusters, and the data from the primed state in Fig. 4B indicate a larger size of clusters in addition to the number. This interpretation is also supported by the data from the primed state, which is an extreme case:  $\sim 5\%$  of the nano-

diffraction patterns contain disc-type diffraction spots, which are produced by nuclei that are large enough to detect but did not grow under the laser irradiation (fig. S5). Patterns from all other amorphous states do not have such spots, and differences in the structural order can only be distinguished by FTEM. [The substrates of the samples shown in Figs. 2 and 4 are optimized for different purposes; consequently, they have different thermal and interfacial characteristics. The longer priming time (4.4  $\mu\text{s}$ ) and cooling time ( $\sim 100$  ns) of the sample in Fig. 4 may induce a higher density of nuclei in the laser-treated state.] Overall, FTEM provides direct evidence that the subcritical nuclei in amorphous AIST increase in size and number after either laser priming or furnace annealing, and they decrease slightly (or maintain) upon melt quenching.

The agreement shown in this work among laser crystallization time, theoretical modeling, and FTEM provides a strong form of proof for the predicted development of subcritical nuclei and their role in the crystallization process. This study establishes FTEM as a powerful method to detect the existence of nanometer-scale nuclei within glassy solids. Such a capability will be an important tool in the further study of the crystallization dynamics in a wide variety of glassy materials. For example, continued development of phase-change memory devices requires the materials to be neither too difficult to crystallize, because this would require excessive transformation power or time, nor too easy to crystallize, because this would compromise long-term data retention by the onset of unwanted crystallization.

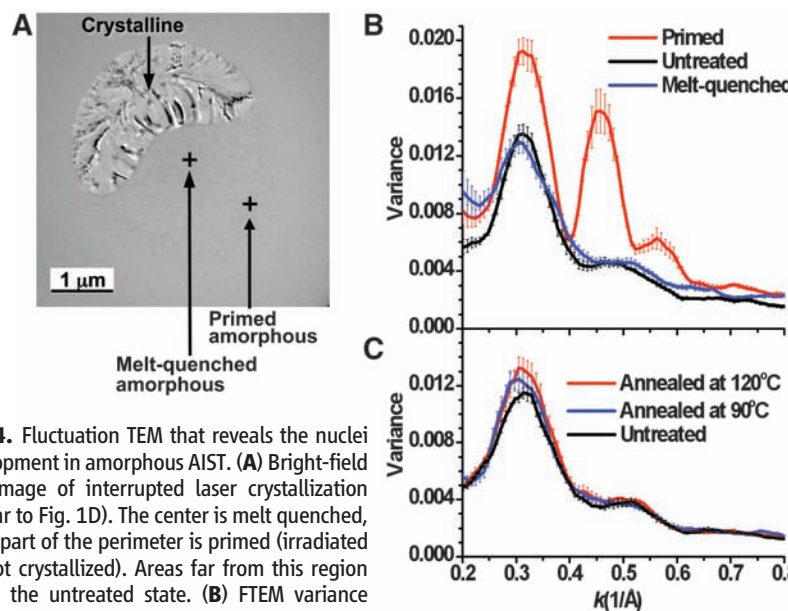


**Fig. 4.** Fluctuation TEM that reveals the nuclei development in amorphous AIST. (A) Bright-field TEM image of interrupted laser crystallization (similar to Fig. 1D). The center is melt quenched, and a part of the perimeter is primed (irradiated but not crystallized). Areas far from this region are in the untreated state. (B) FTEM variance from the untreated, primed, and melt-quenched amorphous states, revealing differences in the population of nuclei; error bars indicate 1 SD of the average (fig. S4). (C) FTEM variance showing the gradual change in nuclei concentration upon low-temperature annealing. Conventional diffraction techniques that use average diffraction intensity cannot distinguish these amorphous states.

#### References and Notes

- J. W. Christian, *The Theory of Transformations in Metals and Alloys: An Advanced Textbook in Physical Metallurgy* (Pergamon, Oxford, ed. 2, 1975).
- K. F. Kelton, in *Solid State Physics*, vol. 45, H. Ehrenreich, D. Turnbull, Eds. (Academic Press, New York, 1991), pp. 75–177.
- D. Kashchiev, *Nucleation: Basic Theory with Applications* (Butterworth Heinemann, Oxford, 2000).
- D. E. Jesson, M. Kastner, B. Voigtlander, *Phys. Rev. Lett.* **84**, 330 (2000).
- I. Goldfarb, *Phys. Rev. Lett.* **95**, 025501 (2005).
- U. Gasser, E. R. Weeks, A. Schofield, P. N. Pusey, D. A. Weitz, *Science* **292**, 258 (2001).
- K.-Q. Zhang, X. Y. Liu, *Nature* **429**, 739 (2004).
- O. L. Krivanek, P. H. Gaskell, A. Howie, *Nature* **262**, 454 (1976).
- M. M. J. Treacy, J. M. Gibson, L. Fan, D. J. Paterson, I. McNulty, *Rep. Prog. Phys.* **68**, 2899 (2005).
- M. M. J. Treacy, J. M. Gibson, *Acta Crystallogr. A* **52**, 212 (1996).
- Materials and methods are available as supporting material on Science Online.
- P. M. Voyles, J. R. Abelson, *Sol. Energy Mater. Sol. Cells* **78**, 85 (2003).
- S. N. Bogle, P. M. Voyles, S. V. Khare, J. R. Abelson, *J. Phys. Condens. Matter* **19**, 455204 (2007).
- J. Wen, Y. Q. Cheng, J. Q. Wang, E. Ma, *J. Appl. Phys.* **105**, 043519 (2009).
- A. L. Greer, N. Mathur, *Nature* **437**, 1246 (2005).
- M. Wuttig, N. Yamada, *Nat. Mater.* **6**, 824 (2007).
- B.-S. Lee, thesis, University of Illinois at Urbana-Champaign (2006).
- M. Salinga, thesis, RWTH, Aachen, Germany (2008).

19. J. Kalb, F. Spaepen, M. Wuttig, *J. Appl. Phys.* **93**, 2389 (2003).  
 20. J. Kalb, F. Spaepen, M. Wuttig, *Appl. Phys. Lett.* **84**, 5240 (2004).  
 21. S. Ziegler, M. Wuttig, *J. Appl. Phys.* **99**, 064907 (2006).  
 22. S. Senkader, C. D. Wright, *J. Appl. Phys.* **95**, 504 (2004).  
 23. J. H. Coombs, A. P. J. M. Jongenelis, W. van Es-Spiekman, B. A. J. Jacobs, *J. Appl. Phys.* **78**, 4906 (1995).  
 24. S. Raoux *et al.*, *IBM J. Res. Dev.* **52**, 465 (2008).  
 25. T. Matsunaga, Y. Umetani, N. Yamada, *Phys. Rev. B* **64**, 184116 (2001).  
 26. R. Bez, R. J. Gleixner, F. Pellizzer, A. Pirovano, G. Atwood, in *Phase Change Materials: Science and Applications*, S. Raoux, M. Wuttig, Eds. (Springer, New York, 2009), pp. 355–380.  
 27. A. N. Pargellis, *J. Vac. Sci. Technol. A* **7**, 27 (1989).  
 28. V. Weidenhof, I. Friedrich, S. Ziegler, M. Wuttig, *J. Appl. Phys.* **89**, 3168 (2001).  
 29. M.-H. Kwon *et al.*, *Appl. Phys. Lett.* **90**, 021923 (2007).  
 30. We thank Y. Xiao, M. Jurich, Y.-C. Chen, M. Salinga, and M. Hitzbleck for their help with thin-film growth and thermal treatments. This material is based on work conducted under IBM-UIUC joint study agreement and is supported by NSF under awards DMR 04-12939 and DMR 07-06267. The FTEM technique was available thanks to collaborative support under award DMR 06-05890. FTEM, AFM, and thermal treatments were carried out, in part, in the Frederick Seitz Materials

Research Laboratory Central Facilities, University of Illinois, which are partially supported by the U.S. Department of Energy under grants DE-FG02-07ER46453 and DE-FG02-07ER46471.

### Supporting Online Material

www.sciencemag.org/cgi/content/full/326/5955/980/DC1  
 Materials and Methods  
 Figs. S1 to S5  
 References

9 June 2009; accepted 11 September 2009  
 10.1126/science.1177483

# Partitioning Recent Greenland Mass Loss

Michiel van den Broeke,<sup>1\*</sup> Jonathan Bamber,<sup>2</sup> Janneke Ettema,<sup>1</sup> Eric Rignot,<sup>3,4</sup> Ernst Schrama,<sup>5</sup> Willem Jan van de Berg,<sup>1</sup> Erik van Meijgaard,<sup>6</sup> Isabella Velicogna,<sup>3,4</sup> Bert Wouters<sup>5,6</sup>

Mass budget calculations, validated with satellite gravity observations [from the Gravity Recovery and Climate Experiment (GRACE) satellites], enable us to quantify the individual components of recent Greenland mass loss. The total 2000–2008 mass loss of ~1500 gigatons, equivalent to 0.46 millimeters per year of global sea level rise, is equally split between surface processes (runoff and precipitation) and ice dynamics. Without the moderating effects of increased snowfall and refreezing, post-1996 Greenland ice sheet mass losses would have been 100% higher. Since 2006, high summer melt rates have increased Greenland ice sheet mass loss to 273 gigatons per year (0.75 millimeters per year of equivalent sea level rise). The seasonal cycle in surface mass balance fully accounts for detrended GRACE mass variations, confirming insignificant subannual variation in ice sheet discharge.

There are strong indications that mass loss from the Greenland ice sheet (GrIS) has recently accelerated (1–3) after atmospheric warming and increased runoff (4, 5) and increased ice discharge through the acceleration of outlet glaciers in the west (6, 7) and east (8–11). Recently reported GrIS mass balance (12) varies from near-balance (13) to modest mass losses [47 to 97 gigatons (Gt) year<sup>-1</sup>] (14) in the 1990s, increasing to a mass loss of 267 ± 38 Gt year<sup>-1</sup> in 2007 (15). These mass losses are equivalent to a global sea level rise (SLR) of 0.13 to 0.74 mm year<sup>-1</sup> or 4 to 23% of the SLR of 3.1 ± 0.7 mm year<sup>-1</sup> reported for the period 1993–2005 (16).

Here we present consistent 2003–2008 GrIS mass loss rates produced by two fully independent methods: The mass budget method, which quantifies the individual components of ice sheet mass balance [surface mass balance (SMB) and ice discharge (D)], is validated with data from the Gravity Recovery and Climate Experiment (GRACE) satellites, which observe ice sheet mass anomalies by repeat satellite gravimetry. This combination of results enables us

to resolve the individual components of recent GrIS mass loss in space and time.

For SMB, we used the monthly output of a 51-year climate simulation (1958–2008) with the Regional Atmospheric Climate Model (RACMO2/GR) at high horizontal resolution (~11 km) (fig. S1). The modeled SMB from RACMO2/GR agrees very well with in situ observations [ $N = 265$ , correlation coefficient ( $r$ ) = 0.95], without need for post-calibration

(17). For D, we used ice flux data from 38 glacier drainage basins (15), covering 90% of the ice sheet (fig. S2), corrected for SMB between flux gate and grounding line and updated to include 2008. To compare SMB-D with GRACE requires the calculation of cumulative SMB-D anomalies. The temporal evolution of the cumulative SMB-D anomaly was evaluated using monthly GRACE mass changes (18). The spatial distribution of GrIS mass changes was compared to a regionally distributed GRACE solution (19), updated to include 2008. For more details on data and methods, see the supporting online material.

Figure 1 compares the time series of the cumulative SMB-D anomaly with GRACE data (18) in the epoch during which both are available (2003–2008). The high correlation ( $r = 0.99$ ) between the two fully independent time series and the similarity in trends support the consistency of the mass balance reconstruction. A linear regression on the SMB-D time series yields a 2003–2008 GrIS mass loss rate of  $-237 \pm 20$  Gt year<sup>-1</sup>.

A potential source of error is that the GRACE signal includes the seasonal cycles of supraglacial/englacial water storage and ice discharge (20–22). Because only a single discharge data point per year is available, we assume slow-

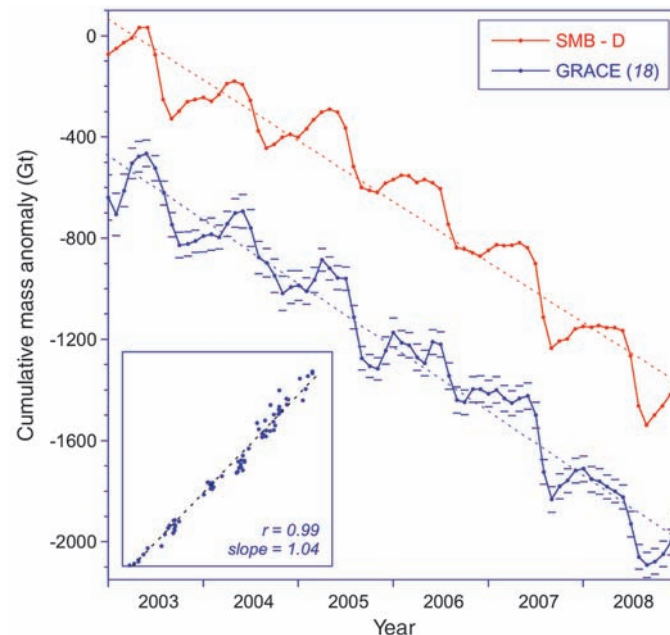


**Fig. 1.** Cumulative SMB-D anomaly (2003–2008) and comparison with GRACE data (18). Short horizontal lines indicate GRACE uncertainty, dashed lines the linear trends. GRACE values are not absolute numbers, and the curve has been vertically shifted for clarity. The scatter plot in the inset shows a direct linear regression between the monthly GRACE values as a function of the cumulative SMB-D anomaly, together with the linear regression coefficients.

<sup>1</sup>Institute for Marine and Atmospheric Research, Utrecht University, Netherlands. <sup>2</sup>Bristol Glaciology Centre, School of Geographical Sciences, University of Bristol, Bristol, UK. <sup>3</sup>Department of Earth System Science, University of California, Irvine, CA, USA. <sup>4</sup>Jet Propulsion Laboratory, Pasadena, CA, USA. <sup>5</sup>Delft Institute of Earth Observation and Space Systems, Delft University of Technology, Delft, Netherlands. <sup>6</sup>Royal Netherlands Meteorological Institute, De Bilt, Netherlands.

\*To whom correspondence should be addressed. E-mail: m.r.vandenbroeke@uu.nl